MAGNETIC SOURCE IMAGING

More than 200 years ago, it was discovered that biological processes are accompanied by electrical currents. Since then, measurements of bioelectric signals have become widespread procedures of great importance in both biophysical research and medical applications in clinical use. These studies include, for example, measurements of electric potential differences arising from human heart [the electrocardiogram (ECG)], brain [the electroencephalogram (EEG)], and other organs.

The same bioelectric activity that generates electrical potentials also generates weak magnetic fields. Because these biomagnetic fields measured outside the body are extremely low in magnitude (~10 fT to 100 pT), it was not until 1963 that the first successful detection of the magnetic field arising from human heart was performed (1). This was the beginning of magnetocardiography (MCG). Magnetoencephalography (MEG) was introduced in 1968 when magnetic signals due to the spontaneous α-rhythm in the brain were detected (2). However, it was only after the development of ultrasensitive superconducting quantum interference device (SQUID) detectors in the beginning of the the 1970s (3) that easier detection of biomagnetic signals became possible. In addition to the magnetocardiogram and the magnetoencephalogram, various biomagnetic fields arising from the body have been studied since then.

Biomagnetic measurements offer information that is very difficult to obtain with other imaging methods (4–8). MEG and MCG are generated by the electric currents in neurons or myocardial cells, and therefore the measurements provide direct real-time functional information about the brain or the heart, respectively. The time scale of the detectable signals ranges from fractions of a millisecond to several seconds or even longer periods. The biomagnetic measurements are totally noninvasive and the body is not exposed to radiation or high magnetic fields. Mapping of biomagnetic signals at several locations simultaneously is easy and fast to perform with multichannel systems.

The metabolic processes associated with the neural or myocardial activity can be studied with positron emission tomography (PET), but the imaging times are several minutes, and the spatial resolution is about 5 mm. Better spatial resolution is obtained from functional magnetic resonance imaging.

Estimation of bioelectric current sources in the body from biomagnetic measurements is often called magnetic source imaging (MSI). To relate the functional information provided by MSI to the underlying individual anatomy, other imaging methods are employed, such as magnetic resonance imaging (MRI), computer tomography (CT), and X ray. In this article, we focus on MEG and MCG, followed by a brief discussion of other fields of biomagnetism. Furthermore, instead of a comprehensive review of MEG and MCG applications we provide a few illustrative examples of recent MSI studies.

MEG AND MCG STUDIES

During recent years, MEG and MCG have attained increasing interest. The ability of these methods to locate current sources combined with precise timing of events is valuable both in basic research and in clinical studies.

One common type of an MEG experiment is to record the magnetic field associated with a sensory stimulus or a movement. Since these fields are usually masked by the ongoing background activity, signal averaging is routinely employed to reveal the interesting signal component. Recordings of neuromagnetic fields have provided a wealth of new information about the organization of primary cortical areas (9).

Sensor arrays covering the whole head have made studies of complicated phenomena involving simultaneous or sequential processing in multiple cortical regions feasible. Because MEG is a unique tool to study information processing in healthy humans, several language-related studies have recently been conducted (10–12).

It is also possible to record the ongoing rhythmic spontaneous brain activity in real time and follow its changes under different conditions (13,14). In addition to the well-known 10 Hz α-rhythm originating in the vision-related cortical areas, similar spontaneous signals occur, for example, in the somatosensory system. MEG measurements have provided new information about both the generation sites of these rhythmic activities and their functional significance (15).

Both evoked responses and spontaneous activity recordings can be utilized in clinical studies (16). For example, the locations of the somatosensory and motor cortices deduced

from evoked MEG signals can be superimposed on three-dimensional surface reconstructions of the brain, computed from MRI data. The resulting individual functional map can be a valuable aid in planning neurosurgical operations. Encouraging results have also been obtained in locating epileptic foci in candidates for epileptic surgery.

High-resolution MCG recordings have been applied both in basic cardiac research and in clinical studies. In the first MCG studies in the 1970s and 1980s, only single-channel devices were available, which limited the use of MCG to subjects and patients with normal sinus rhythm. Introduction of multichannel recording systems in the 1990s made the technique more suitable for routine clinical studies and for analysis of beat-to-beat variations. Currently, MCG is being used at some hospitals to test and further develop its clinical use.

Multichannel MCG studies are particularly promising in two clinically important problems: (1) in locating noninvasively abnormal cardiac activity critical for the arousal of life-threatening arrhythmias and (2) in evaluating the risk of such arrhythmias in different cardiac pathologies, especially after myocardial infarction. Successful MCG results have been reported, for example, in locating abnormal ventricular preexcitation sites associated with the Wolff–Parkinson–White syndrome, the origin of ventricular extrasystolic beats, and the origin of focal atrial tachycardias (17–21).

Furthermore, MCG localization accuracy has been tested with artificial sources, such as a pacing catheter in the heart (20,22). The localization accuracy reported so far, ranging from about 5 mm to 25 mm, is sufficient to provide valuable information for preablative evaluation of the patients. In addition to localization studies, MCG has been applied to retrospective identification of patients prone to malignant arrhythmias with about 90% sensitivity and specificity (23).

INSTRUMENTATION

Detection of Neuromagnetic Fields

The detector that offers the best sensitivity for the measurement of these tiny fields is the SQUID (24,25), which is a superconducting ring, interrupted by one or two Josephson junctions (26). These weak links limit the flow of the supercurrent, which is characterized by the maximum critical current I_c that can be sustained without loss of superconductivity. Direct-current (dc) SQUIDs, with two junctions, are preferred because the noise level is lower in them than in radio-frequency (RF) SQUIDs (27–29).

The magnetic signals from the body are extremely weak compared with ambient magnetic field variations (5) Thus, rejection of outside disturbances is of utmost importance. Significant magnetic noise is caused, for example, by fluctuations in the earth's geomagnetic field, by moving vehicles and elevators, and by the omnipresent powerline fields.

For rejection of external disturbances, biomagnetic measurements are usually performed in a magnetically shielded room. To make such an enclosure, four different methods exist: Ferromagnetic shielding, eddy-current shielding, active compensation, and the recently introduced high-T_c superconducting shielding. Many experimental rooms have been built for biomagnetic measurements utilizing combinations of these techniques (34–36). Commercially available rooms utilized in biomagnetic measurements usually employ two layers of aluminum and ferromagnetic shielding, possibly combined with active compensation. The inside floor area is usually 3 m by 4 m, and the height around 2.5 m.

In addition, the sensitivity of the SQUID measuring system to external magnetic noise can be greatly reduced by the proper design of the flux transformer, a device normally used for bringing the magnetic signal to the SQUID. For example, an axial first-order gradiometer consists of a pickup (lower) coil and a compensation coil with identical effective area and connected in series but wound in opposition [see Fig. 1(a)]. This system of coils is insensitive to a spatially uniform background field, but it responds to inhomogeneities. Therefore, a source near the lower coil, which will cause a much greater field in the pickup loop than in the more remote compensation coil, will thus produce a net output.

Most biomagnetic measurements have been performed with axial gradiometers. However, the off-diagonal planar configuration of Fig. 1(b) has some advantages over axial coils: The double-D construction (30) is compact in size, and it can be fabricated easily with thin-film techniques. The locating accuracies of planar and axial gradiometer arrays are essentially the same for superficial sources (31–33). The spatial sensitivity pattern, lead field, of off-diagonal gradiometers is narrower and shallower than that of axial gradiometers. These sensors thus collect their signals from a more restricted area near the sources of interest, and there is less overlap between lead fields of adjacent sensors in a multichannel array.

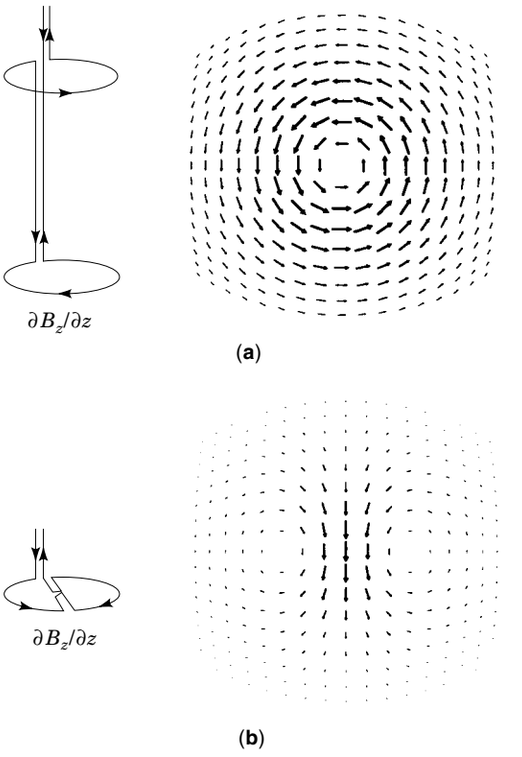

Figure 1. Left: Coil configurations for (a) an axial and (b) a planar gradiometer. Right: The corresponding sensitivity patterns, lead fields (see section entitled "Distributed Source Models."). The plots show the lead fields on a spherical surface. The gradiometer coil is located above the center of each pattern. The direction and size of the arrows indicate the magnitude and direction of the lead field at the center of the arrow.

Nevertheless, distant sources can often be detected more easily with axial gradiometer or magnetometer sensors. Therefore, many experimental and commercial systems include these coil configurations, possibly in combination with planar gradiometers.

Multichannel Magnetometers

The first biomagnetic measurements were performed with single-channel instruments. However, reliable localization of current sources requires mapping in several locations, and this is time-consuming with only one channel. Besides, unique spatial features present in, for example, brain rhythms cannot be studied. Fortunately, during the past 15 years, multichannel SQUID systems for biomagnetic measurements have been developed to provide reliable commercial products. A detailed account of this development can be found in Ref. 5.

A state-of-the-art multichannel MEG system comprises more than 100 channels in a helmet-shaped array to record the magnetic field distribution across the brain simultaneously. The latest MCG systems contain 60 to 80 detectors in a flat or slightly curved array to cover an area about 30 cm in diameter over the subject's chest or back. The dewar containing the sensors is attached to a gantry, which allows easy positioning of the dewar above the subject's head or chest. The position of the dewar with respect to the subject's head or torso is typically determined by measuring the magnetic field arising from an ac current fed into small marker coils attached to the skin (37,38) and by calculating their locations with respect to the sensor array. The locations of the marker coils with respect to an anatomical frame of reference are determined before the biomagnetic measurement by a three-dimensional digitizer.

As an example of an MEG installation we describe the Neuromag-122 system (Neuromag Ltd., Helsinki, Finland) (33). This device employs planar first-order two-gradiometer units to measure the two off-diagonal derivatives, $\partial B_z/\partial x$ and $\partial B_z/\partial y$, of B_z, the field component normal to the dewar bottom at 61 locations. The thin-film pickup coils are deposited on 28×28 mm^2 silicon chips; they are connected to 122 dc SQUIDs attached to the coil chip. The separation between two double-sensor units is about 43 mm. The system is depicted in Fig. 2.

The MCG system from the same company shown in Fig. 2 comprises 67 channels arranged on a slightly curved surface with diameter about 30 cm. The magnetic-field component (B_z) perpendicular to the sensor array surface is sensed by seven large-coil axial gradiometers and 30 two-channel planar gradiometer units identical to those described in the previous paragraph.

GENERATION OF BIOELECTROMAGNETIC FIELDS

Cellular Sources

To interpret the measured signals, one has to understand how electric and magnetic fields are generated by biological tissue. In this article, we consider biomagnetic signals generated by the electric currents in excitable tissue. These magnetic fields are linked to bioelectric potentials, and it is useful to consider both the magnetic field and the electric potential together.

Living cells sustain a potential difference between intra- and extracellular media. In a static situation, most cells are, as seen externally, electrically and magnetically silent. Excitable cells can produce electric surface potentials and external magnetic fields, which can be detected from outside.

The Quasi-Static Approximation

The total electric current density in the body, $\boldsymbol{J}$, is time-dependent, and the electric field ($\boldsymbol{E}$) and the magnetic field ($\boldsymbol{B}$) produced by $\boldsymbol{J}$ can be found from Maxwell's equations. However, the variations in time are relatively slow (below 1 kHz) (8,39), which allows treatment of the sources and the fields in a quasi-static approximation. This means that inductive, capacitive, and displacement effects can be neglected. In the quasi-static approximation Maxwell's equations thus read:

$$\nabla \cdot \boldsymbol{E} = \rho/\epsilon_0 \tag{1}$$

$$\nabla \times \boldsymbol{E} = 0 \tag{2}$$

$$\nabla \cdot \boldsymbol{B} = 0 \tag{3}$$

$$\nabla \times \boldsymbol{B} = \mu_0 \boldsymbol{J} \tag{4}$$

where μ_0 and ϵ_0 are the magnetic permeability and electric permittivity of the vacuum, respectively.

Primary Current

It is useful to divide the total current density in the body, $\boldsymbol{J}(\boldsymbol{r})$, into two components. The passive volume or return current is proportional to the conductivity $\sigma(\boldsymbol{r})$ and the electric field $\boldsymbol{E}$:

$$\boldsymbol{J}^{\mathrm{v}}(\boldsymbol{r}) = \sigma(\boldsymbol{r})\boldsymbol{E}(\boldsymbol{r}) \tag{5}$$

$\boldsymbol{J}^{\mathrm{v}}$ is the result of the macroscopic electric field on charge carriers in the conducting medium. Everything else is the primary current $\boldsymbol{J}^{\mathrm{p}}$:

$$\boldsymbol{J}(\boldsymbol{r}) = \boldsymbol{J}^{\mathrm{p}}(\boldsymbol{r}) + \sigma(\boldsymbol{r})\boldsymbol{E}(\boldsymbol{r}) \tag{6}$$

This definition would be meaningless without reference to the length scale. Here $\sigma(\boldsymbol{r})$ is the macroscopic conductivity; cellular-level details are left without explicit attention. The division in Eq. (6) is illustrative in that neural or cardiac activity gives rise to primary current mainly inside or in the vicinity of a cell, whereas the volume current flows passively everywhere in the medium.

It should be emphasized that $\boldsymbol{J}^{\mathrm{p}}$ is to be considered the driving "battery" in the macroscopic conductor; although the conversion of chemical gradients to current is due to diffusion, the primary current is largely determined by the cellular-level details of conductivity. In particular, the membranes, being good electrical insulators, guide the flow of both intracellular and extracellular currents.

If the events are considered on a cellular level, it is customary to speak about the impressed rather than primary current (39).

Neurons

Signals propagate in the brain along nerve fibers called axons as a series of action potentials. During an action potential, the primary current can be approximated by a pair of current

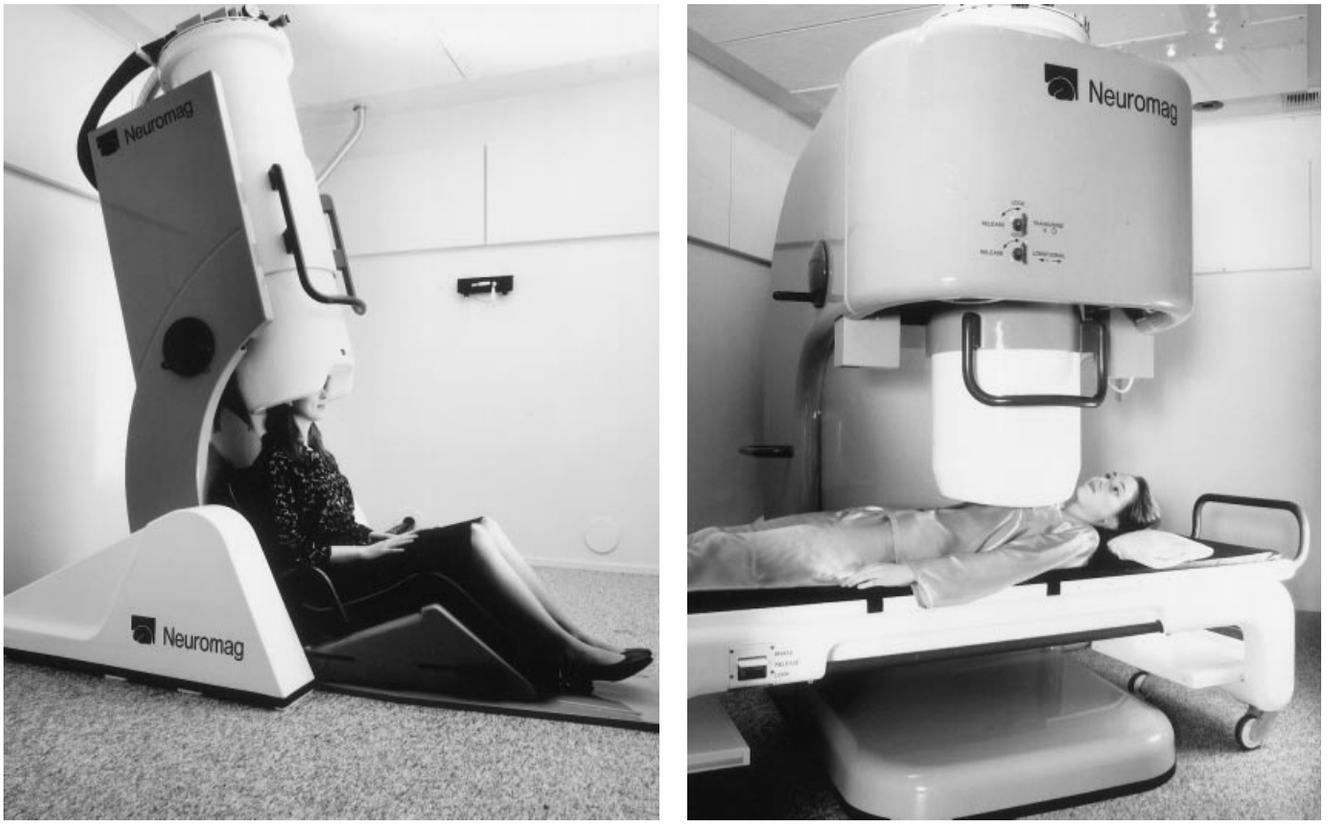

Figure 2. Left: The Neuromag-122™ MEG system. Right: The 67-channel MCG system. (Photographs courtesy of Neuromag, Ltd.)

dipoles corresponding to a local depolarization of the cell membrane, followed by repolarization. This source moves along the axon as the activation propagates. Although the model is a simplified one, the experimental magnetic findings are in reasonable agreement with this concept (40,41).

The axons connect to other neurons through synapses. In a synapse, transmittter molecules are released to the synaptic cleft and attach to the receptors on the postsynaptic cells. As a result, the ionic permeabilities of the postsynaptic membrane are modified and a postsynaptic potential is generated. The postsynaptic current can be adequately described by a single-current dipole.

The dipolar field produced by the postsynaptic current flow falls off with distance more slowly than the quadrupolar field associated with the action potentials. Furthermore, the postsynaptic currents last tens of milliseconds, whereas the duration of a typical action potential is only about 1 ms. On this basis, it is believed that that the electromagnetic signals observed outside and on the surface of the head are largely due to the synaptic current flow.

The two principal groups of neurons on the surface layer of the brain, the cortex, are the pyramidal and the stellate cells. The former are relatively large; their apical dendrites from above reach out parallel to each other, so that they tend to be perpendicular to the cortical surface. Since neurons guide the current flow, the resultant direction of the electrical current flowing in the dendrites is also perpendicular to the cortical sheet of gray matter.

Myocardium

In heart tissue, there are three main types of cells: pacemaker cells in the sinus and atrioventricular nodes, cells specialized for rapid conduction of the excitation along the bundle of His and Purkinje network, and, finally, muscle cells that perform mechanical work. Cardiac muscle consists of a large number of individual cells, each about 15 μm in diameter and 100 μm long. The intracellular spaces of adjacent muscle cells are interconnected, which makes the three-dimensional structure very complex.

An action potential in myocardial cells lasts 300 ms to 400 ms, which is over 100 times longer than a typical neural action potential. Provided that we observe a single myocardial cell at some distance from the membrane, the depolarization and repolarization can be modeled, respectively, by an equivalent depolarization and repolarization dipole.

Ventricular depolarization or repolarization propagates as about 1 mm thick wavefronts in the heart. A commonly used model to describe such propagating fronts is a uniform double layer (39). It consists of dipoles with equivalent strengths (assuming a constant dipole density), oriented perpendicular to the wavefront. The model is more suitable than a single current dipole in characterizing an excitation taking place simultaneously in a spatially large region, but it cannot account for possible holes in the wavefront (e.g., necrotic tissue). In addition, the classical concept of a uniform double layer is not valid if the anisotropic nature of myocardial tissue is to be included.

Calculation of the Bioelectromagnetic Fields

In the quasi-static approximation, the electric potential ϕ obeys Poisson's equation:

$$\nabla \cdot (\sigma \nabla \phi) = \nabla \cdot \boldsymbol{J}^{\mathrm{p}} \tag{7}$$

while the magnetic field due to the total current density, $\boldsymbol{J}$, is obtained from the Ampère–Laplace law:

$$\boldsymbol{B}(\boldsymbol{r}) = \frac{\mu_o}{4\pi} \int_V \frac{\boldsymbol{J}(\boldsymbol{r}') \times \boldsymbol{R}}{R^3}\, dv' \tag{8}$$

where the integration is performed over a volume V containing all active sources, $\boldsymbol{r}' \in V$, $\boldsymbol{R} = \boldsymbol{r} - \boldsymbol{r}'$.

It can be shown that the volume currents in an infinite homogeneous volume conductor give no contribution to the electric potential or the magnetic field, which are solely due to the primary currents, $\boldsymbol{J}^{\mathrm{p}}$ (42).

Next, we assume that the body consists of homogeneous subvolumes v_k', $k = 1, 2, \ldots, M$, bounded by the surfaces S_k. The electrical conductivity within v_k' is constant, σ_k. Usually, the body is surrounded by air, and thus the conductivity outside the body surface is zero. In this case, the surface potential, ϕ_{S}, can be obtained from an integral equation (43)

$$(\sigma_l'' + \sigma_l')\phi_{\mathrm{S}}(\boldsymbol{r}) = 2\sigma_n \phi_\infty(\boldsymbol{r}) + \frac{1}{2\pi} \sum_{k=1}^{M} (\sigma_k'' - \sigma_k') \int_{S_k} \phi_{\mathrm{S}}\, d\boldsymbol{S}_k \cdot \frac{\boldsymbol{R}}{R^3} \tag{9}$$

where σ_n is the conductivity at the source location, σ_k' is the conductivity inside and σ_k'' is the conductivity outside the surface S_k, and $d\boldsymbol{S}_k$ is the surface element vector perpendicular to the boundary. The term ϕ_∞ denotes the electric potential in an infinite homogeneous medium (in the absence of the boundaries S_k), and the surface integral accounts for the contribution of the counductivity change on the boundary S_k.

The external magnetic field is then evaluated by substituting the total current density, $\boldsymbol{J}$, into Eq. (8). It can be shown (44) that the result can be transformed to the form

$$\boldsymbol{B}(\boldsymbol{r}) = \boldsymbol{B}_\infty(\boldsymbol{r}) + \frac{\mu_o}{4\pi} \sum_{k=1}^{M} (\sigma_k'' - \sigma_k') \int_{S_k} \phi_{\mathrm{S}}\, d\boldsymbol{S}_k \times \frac{\boldsymbol{R}}{R^3} \tag{10}$$

where the term $\boldsymbol{B}_\infty$ is the magnetic field in the absence of the boundaries, S_k. Again, the surface integral accounts for the contribution of the counductivity change on the boundary S_k.

Analytic Solutions. Analytic solutions of Eqs. (9) and (10) exist only in a few simple symmetric geometries. If we approximate the head or the torso by a layered spherically symmetric conductor, it is possible to derive a simple analytic expression for the magnetic field of a current dipole (41):

$$\boldsymbol{B}(\boldsymbol{r}) = \frac{\mu_0}{4\pi} \frac{F\boldsymbol{Q} \times \boldsymbol{r}_Q - (\boldsymbol{Q} \times \boldsymbol{r}_Q \cdot \boldsymbol{r}) \nabla F(\boldsymbol{r}, \boldsymbol{r}_Q)}{F(\boldsymbol{r}, \boldsymbol{r}_Q)^2} \tag{11}$$

where $\boldsymbol{r}_Q$ is the location of the current dipole, $\boldsymbol{Q}$ is the dipole moment vector, $F(\boldsymbol{r}, \boldsymbol{r}_Q) = a(ra + r^2 - \boldsymbol{r}_Q \cdot \boldsymbol{r})$, and $\nabla F(\boldsymbol{r}, \boldsymbol{r}_Q) = (r^{-1}a^2 + a^{-1}\boldsymbol{a} \cdot \boldsymbol{r} + 2a + 2r)\boldsymbol{r} - (a + 2r + a^{-1}\boldsymbol{a} \cdot \boldsymbol{r})\boldsymbol{r}_Q$, with $\boldsymbol{a} = (\boldsymbol{r} - \boldsymbol{r}_Q)$, $a = |\boldsymbol{a}|$, and $r = |\boldsymbol{r}|$.

An important feature of the sphere model is that the result is independent of the conductivities and thicknesses of the layers; it is sufficient to know the center of symmetry. The calculation of the electric potential is more complicated: The results can be expressed only as a series expansion of Legendre polynomials, and full conductivity data are required (45). Furthermore, radial currents do not produce any magnetic field outside a spherically symmetric conductor. Thus MEG is, to a great extent, selectively sensitive to tangential sources, and EEG data are required to recover all components of the current distribution.

The obvious advantage of a simple forward model is that a fast analytical solution is available. It has also been shown (46) that a sphere model fitted to the local curvature of the skull's inner surface (4) provides accurate enough estimates for many practical purposes. However, when the source areas are located deep within the brain or in the frontal lobes, it is necessary to use more accurate approaches.

In the first MCG localization studies the body was approximated as a homogeneous semi-infinite space, which can be regarded as a generalization of a spherical model with the radius extended to infinity (47,48).

However, later computer studies have shown that the semi-infinite approximation is oversimplified, and a more accurate description of the thorax shape is needed in the inverse studies (21,49). A slightly more accurate description of the thorax geometry can be obtained by using cylindrical or spheroidal models. However, the analytical expressions for arbitrary dipolar sources become substantially more complex than in the spherical case (50), and only a few studies to apply spheroids have been reported.

Numerical Approaches. When a realistic geometry of the head or the thorax is taken into account, numerical techniques are needed to solve the Maxwell equations. When applying the boundary-element method (BEM), electric potential and magnetic field are calculated from the (quasi-static) integral equations [Eqs. (9) and (10)], which can be discretized to linear matrix equations (46,49,51).

In most BEM applications to the bioelectromagnetic forward problem, the surfaces are tessellated with triangular elements, assuming either constant or linear variation for the electric potential on each triangle. However, the accuracy of the magnetic-field computation may suffer if a dipole source is located near a triangulated surface. The accuracy can be improved, for example, by applying Galerkin residual weighting instead of the standard collocation method and by approximating the surfaces with curved elements instead of plane triangles (52).

Realistically shaped geometries of each subject are usually extracted from MRI data. The regions of interest (e.g., the heart, the lungs, and the thorax; or the brain, the skull, and the scalp) need to be segmented from the data first (see section entitled MRI). The volumes or the surfaces are then discretized for numerical calculations. The segmentation and tessellation problems are still tedious and nontrivial (53).

The relatively low conductivity of the skull greatly facilitates the modeling of MEG data. In fact, a highly accurate model for MEG is obtained by considering only one homogeneous compartment bounded by the skull's inner surface (46). With suitable image processing techniques it is possible to

isolate this surface from high-contrast MRI data with little or no user intervention.

The boundary-element model is more complex for EEG, because three compartments need to be considered: the scalp, the skull, and the brain. While the surface of the head can be easily extracted from the MRI data, it is difficult to construct a reliable algorithm to automatically isolate the scalp-skull boundary. In addition, special techniques are required to circumvent the numerical problems introduced by the high conductivity contrast due to the low-conductivity skull.

It is also possible to employ the finite-element method (FEM) or the finite-difference method (FDM) in the solution of the forward problem. The solution is then based on the discretization of Eq. (7). In this case, any three-dimensional conductivity distribution and even anisotropic conductivity can be incorporated (54). However, the solution is more time-consuming than with the BEM, and therefore the FEM or FDM has not been used in routine source modeling algorithms which require repeated calculation of the magnetic field from different source distributions.

SOURCE MODELING

The Inverse Problem

The goal of the bioelectric (EEG, ECG) and biomagnetic (MEG, MCG) inverse problems is to estimate the primary source current density underlying the electromagnetic signals measured outside or on the surface of the body. Unfortunately, the primary current distribution cannot be recovered uniquely, even if the electric potential and the magnetic field were known precisely everywhere at the surface and outside the body (55). However, it is often possible to use additional anatomical and physiological information to constrain the problem and facilitate the solution. One can also replace the actual current sources by equivalent generators that are characterized by a few parameters. The values of the parameters can then be uniquely determined from the measured data by a least-squares fit. The solution of the forward problem is a prerequisite for dealing with the inverse problem requiring repeated solution of the forward problem.

The Current Dipole Model. The simplest physiologically sound model for the neural or myocardial current distribution comprises one or several point sources, current dipoles. In the simplest case the field distribution, measured at one time instant, is modeled by that produced by one current dipole. The best-fitting *equivalent current dipole* (ECD) can be found by using standard least-squares optimization methods such as the Levenberg–Marquardt algorithm (56).

In the time-varying dipole model, introduced by Scherg and von Cramon (57,58), an epoch of data is modeled with a set of dipoles whose orientations and locations are fixed but whose amplitudes vary with time. Each dipole corresponds to a small patch of cerebral cortex or other structures activated simultaneously or in a sequence. The precise details of the current distribution within each patch cannot be revealed by the measurements, which are performed at a distance in excess of 3 cm from the sources.

As a result of the modeling, one obtains the locations of the sources and the orientation of the dipole component tangential to the inner surface of the overlying skull. In addition, traces of the evolution of the source strengths are obtained. Again, the optimal source parameters are found by matching the measured data collected over a period of time with those predicted by the model using the least-squares criterion.

From a mathematical point of view, finding the best-fitting parameters for the time-varying multidipole model is a challenging task. Because the measured fields depend nonlinearly on the dipole position, the standard least-squares minimization routines may not yield the globally optimal estimates. Therefore, global optimization algorithms (59) and special fitting strategies (60), taking into account the physiological characteristics of particular experiments, have been suggested. For each candidate set of dipole positions and orientations it is, however, straightforward to calculate the optimal source amplitude waveforms using linear least-squares optimization methods (61).

In cardiac studies, an ECD is applicable for approximating the location and strength of the net primary current density confined in a small volume of tissue. Myocardial depolarization initiated at a single site spreads at a velocity of about 0.4 mm/ms to 0.8 mm/ms, and the ECD can be thought to be moving along the "center of mass" of the excitation. In practice, localization based on a single ECD is meaningful only during the first 10 ms to 20 ms of excitation.

Because both nonlinear fits for spatial coordinates and linear fits for dipole moment parameters need to be searched at every time instant, the use of even two ECDs becomes very complicated in cardiac studies. Alternatively, cardiac excitation can be modeled with a set of spatially fixed stationary or rotating dipoles, but attempts to define the time courses of the dipole magnitudes usually result in physiologically unacceptable results.

The Current Multipole Expansion. It is often convenient to present the electric potential and the magnetic field as multipole expansions. In the current multipole expansion the field due to the primary current, $\boldsymbol{B}_\infty$ in Eq. (10), is expressed as a Taylor series (62). Thus, more complex source current configurations can be described as higher-order multipole moments, such as quadrupole moments.

Different source models can be built by combining dipole and quadrupole moments. A current dipole is actually the lowest-order term in a general current multipole expansion (62); higher-order terms, such as quadrupoles and octupoles, can be used to account for more complex primary current configurations (48).

Distributed Source Models. Another approach often taken in source modeling is to relax the assumptions on the sources and use various estimation techniques to yield a distributed image of the sources. These methods include, for example, the minimum-norm estimates (63), magnetic-field tomography (MFT) (64), and low-resolution electromagnetic tomography (LORETA) (65).

The source images can provide reasonable estimates of complex source configurations without having to resort to complicated multidipole fitting strategies. However, one must keep in mind that even if the actual source is pointlike, its image is typically blurred, extending a few centimeters in each linear dimension. Therefore, the size of the "blobs" in the source images does not directly relate to the actual dimen-

sions of the source but rather reflects an intrinsic limitation of the imaging method.

The basic concept relevant to all distributed source estimation methods is the lead field. The signal b_k detected by the kth sensor in the sensor array is a linear functional of the primary current distribution $\boldsymbol{J}^{\mathrm{p}}$ and can be expressed as

$$b_k = \int_G \boldsymbol{L}_k(\boldsymbol{r}) \cdot \boldsymbol{J}^{\mathrm{p}}(r)\, dv \tag{12}$$

where the integration extends over the source region G, which can be a curve, a surface, or a volume. The functions $\boldsymbol{L}_k$ are often called lead fields, which can be readily obtained by solving the forward problem for dipole sources.

The minimum-norm estimate (63) is the current distribution that has the smallest norm and is compatible with the measured data. Here, the norm is defined by

$$\|\boldsymbol{J}\|^2 = \int_G J(\boldsymbol{r})^2\, dv \tag{13}$$

The minimum-norm estimate $\boldsymbol{J}^*$ can be expressed as a weighted sum of the lead fields, $\boldsymbol{J}^* = \sum_{k=1}^{N} w_k \boldsymbol{L}_k$. The weighting coefficients are found by fitting the data, computed from the minimum-norm estimate with those actually measured. Since the lead fields in a large array are almost linearly dependent, regularization techniques are needed to produce stable estimates.

Another type of a distributed source model was developed for reconstructing the sequence of ventricular depolarization by van Oosterom et al. (66). Their model is based on a uniform double layer of constant strength. Lead fields for MCG and ECG sensors are evaluated at each node on the endo- and epicardial surfaces of the heart. These transfer functions are weighted by the Heaviside time step function to define the onset of excitation at each surface node. Physiological constraints and regularization are then applied to limit the number of solutions.

Regularization and Constraints

The bioelectromagnetic forward problem can be written as $\boldsymbol{b} = \boldsymbol{L}\boldsymbol{x} + \boldsymbol{e}$, where vector $\boldsymbol{x}$ represents the unknown (linear and nonlinear) source parameters, vector $\boldsymbol{b}$ consists of the measured (MEG/EEG or MCG/ECG) signals, vector $\boldsymbol{e}$ contains the contribution of measurement noise, and matrix $\boldsymbol{L}$ is effectively the transfer (lead field) function between the sources and the measurement sensors. Even small contributions of the noise $\boldsymbol{e}$ make the solution for $\boldsymbol{x}$ very ill-posed. Therefore, regularization techniques are needed to stabilize the solution (67).

In bioelectromagnetic studies dealing with source distributions, the most frequently applied techniques include the truncated-eigenvalue singular value decomposition (63) and the L-curve method (67). Another new approach is based on Wiener filtering and orthogonalized lead fields (68). In addition, spatial weighting can be applied to improve the solutions (21,69). Futher improvements are achieved by applying more than one constraint at the same time (70).

One can also make explicitly the additional assumption that the activated areas have a small spatial extent. For example, the MFT algorithm obtains the solution as a result of an iteration in which the probability weighting is based on the previous current estimate (64). According to the authors, this procedure produces more focal images than the traditional minimum-norm solutions. Another possibility is to use a MUSIC-type probability weighting (61) combined with cortical constraints to focus the image (71).

An approach that incorporates the desire to procure focal source images is to use the L^1 norm, that is, the sum of the absolute values of the current over the source space, as the criterion to select the best current distribution among those compatible with the measurement (72–74). In contrast to the traditional L^2-norm cost function [see Eq. (13)], the L^1-norm criterion yields estimates focused to a few small areas within the source space.

The most powerful way to constrain the bioelectromagnetic inverse problem is to apply anatomical and functional *a priori* information. For example, accurate reconstruction of the cortex surface or myocardial tissue from MRI data limits the spatial extent and orientation of the sources (75). Solutions can also be made more robust by requiring temporal smoothness. Invasively recorded signals such as intraoperative potential recordings from the cortex or from the heart can also be very valuable in developing proper physiological and temporal constraints for distributed sources.

The Relation between Bioelectric and Biomagnetic Signals

Both bioelectric and biomagnetic fields are generated by the same activity. As a consequence, there must be a correlation both in the temporal waveforms and in the spatial maps of the measured signals. Therefore, it is evident that bioelectric and biomagnetic measurements reveal partly redundant information. However, neither one can be used to uniquely reproduce the other; there are current configurations that produce either electric or magnetic field, but not both. A practical example of a magnetically silent source is a radial dipole in a spherically symmetric conductor. On the other hand, solenoidal currents do not produce any electric potential. This may become important, for example, in cardiac exercise studies (76). Therefore, a combination of magnetic and electric recordings seems appealing to obtain more complete information about the current distributions. Still, few attempts to combine electric and magnetic data have been reported (21,58,77,78).

In the previous considerations it was assumed that the volume conductor is homogeneous or piecewise homogeneous. However, many biological tissues are organized directionally, and the electrical conductivity depends on the direction of the fibers. For example, the conductivity in myocardial fibers is about three times higher in the main fiber direction than across the fibers. Colli-Franzone et al. (79) showed that a classical uniform dipole layer, as representing the myocardial wavefront, should be revised to take into account the anisotropic nature of the tissue. They were able to explain experimentally measured potential distributions with an oblique dipole layer, where the dipoles may also have tangential components in addition to the normal component.

Wikswo (80) studied isolated animal preparations and employed microSQUIDs and microelectrodes to measure magnetic and electric fields during and after applying a current stimulus. According to their results, the magnetic field is more sensitive to the underlying anisotropy than the electric potential. With such combined electric and magnetic re-

cordings, it is at least in principle possible to determine the intra- and extracellular conductivity values.

The anisotropic properties of the heart are especially evident near the ventricular apex, where the spiral arrangements of the myocardial fibers can be observed on the epicardial surface. It has been argued that this kind of vortex geometry leads to electrically silent components in magnetic field. However, van Oosterom et al. (66) arrived at the conclusion that the anisotropy does not play a significant role in the ECG or MCG during the normal ventricular depolarization. On the other hand, the findings of Brockmeier et al. (76) in pharmacological MCG stress testing indicate that the anisotropy may cause larger repolarization changes in multichannel MCG signals than in the simultaneously recorded ECG maps.

The tissue is directionally oriented also in the brain. For example, the conductivity of the white matter in the direction of the fibers may be 10 times higher than the conductivity across the fibers. In the cerebral cortex, the corresponding factor is about two. In general, the anisotropy influences the body surface potentials and magnetic fields. However, in the sphere model a difference between the radial and the two tangential conductivities does not affect the magnetic field, while the influence on the electric potential is still substantial.

INTEGRATION WITH OTHER IMAGING MODALITIES

Fast high-field MRI devices provide precise anatomical data. Besides reconstruction of accurately shaped volume-conductor models, anatomic MRI data on the heart and the brain are necessary to combine the inverse solutions with the anatomy in a clinically useful presentation. Examples of source displays of both MRI slices and three-dimensional surface reconstructions are shown in the section entitled "Applications."

Segmentation of the structures of interest from image data is presently the most time-consuming part in constructing individualized boundary element models. In the medical imaging field, accurate extraction of anatomic structures from image data sequences is still an open problem. In practice, manual extraction of the objects of interest—for example, from MRI slices—is often considered the most reliable technique.

Recently, automated region-based and boundary-based segmentation and triangulation methods have been developed, for example, for extracting the lungs, heart, and thorax, or the brain and skull. In region-based methods, some features based on the intensity of the images are used to merge voxels. The boundary-based methods, in turn, rely on an intensity gradient detection. Both methods have limitations, but the utilization of prior geometrical knowledge, such as triangulated surfaces generated from data on other subjects, provides useful additional information. For example, a deformable pyramid model can then provide automatic segmentation and triangulation of the anatomic objects (53,81).

MRI is still fairly expensive, especially for large patient populations. Thus, methods are being developed to use other imaging methods for reconstructing individualized triangulated surfaces. In cardiac studies, two orthogonal thorax X-ray projections, or ultrasound images of the heart combined with three-dimensional (3D) digitization of the thorax surface, can be utilized to acquire patient-specific geometry models.

In principle, CT images could be used instead of MRI to construct a boundary-element model of the head. The skull is particularly easy to isolate from these data. However, the classification of soft tissues is often easier from MR images and the radiation load imposed by a CT scan is generally considered too high for healthy subjects.

To present the MEG/MCG inverse solutions accurately on the individual anatomy, special care needs to be taken with regard to combining the different coordinate frames. Prior to biomagnetic recordings, one has to fix some marker points, for example, with a 3-D digitization system. During MRI or X-ray imaging, specific markers clearly visible and identifiable, such as vitamin pills or tubes filled with MgCl solution, are attached on the reference points. Three or more markers are usually required to achieve sufficient accuracy in the data fusion.

Functional MRI perfusion studies of ischemic or infarcted heart are particularly valuable in developing physiological constraints and in validating the MCG/ECG localization results of ischemia or arrhythmogenic tissue. In brain studies, new possibilities are opened by combining the millimeter-level spatial resolution of functional MRI and the millisecond-scale temporal resolution of MEG and EEG. Weighting of minimum-norm solutions by functional MRI voxel information has been applied, for example, in visual stimulation studies (82).

However, it must be taken into account that fMRI and biomagnetic measurements are not always detecting common activity. Very clear changes of electric and magnetic signals can be easily missed by fMRI if they occur rarely or are very transient thus producing relatively small average changes in the metabolic level. Furethermore, all experimental setups cannot be easily used in both biomagnetic and fMRI studies. It may thus be necessary to often compare the final results of the analysis of each modality rather than aiming at a combination during the source reconstruction.

It is also possible to utilize positron emission tomography (PET) studies in combination with the electromagnetic methods. However, PET imposes a radiation load on the subject, and therefore the possibilities to perform multiple studies on a given subject are limited. Furthermore, PET is available only in a few centers, whereas MRI systems capable of functional imaging are generally available in modern hospitals.

APPLICATIONS

Brain Studies

Auditory Evoked Fields. Fig. 3 shows the results of a typical auditory evoked-response study performed with a whole-head MEG instrument (83). The responses were elicited by 50 ms tones delivered every 4 s to the subject's right ear. The data were averaged over about 100 repetitions with the stimulus onset as a trigger.

The signals were modeled with two current dipoles in a spherically symmetric conductor. The optimal locations, orientations, and time courses of the dipoles were determined with a least-squares search. Fig. 3 shows the averaged data, the distribution of the magnetic field component normal to the measurement surface at the peak signal value, the time courses of the source amplitudes, and the locations of the sources superimposed on a 3-D surface rendering computed

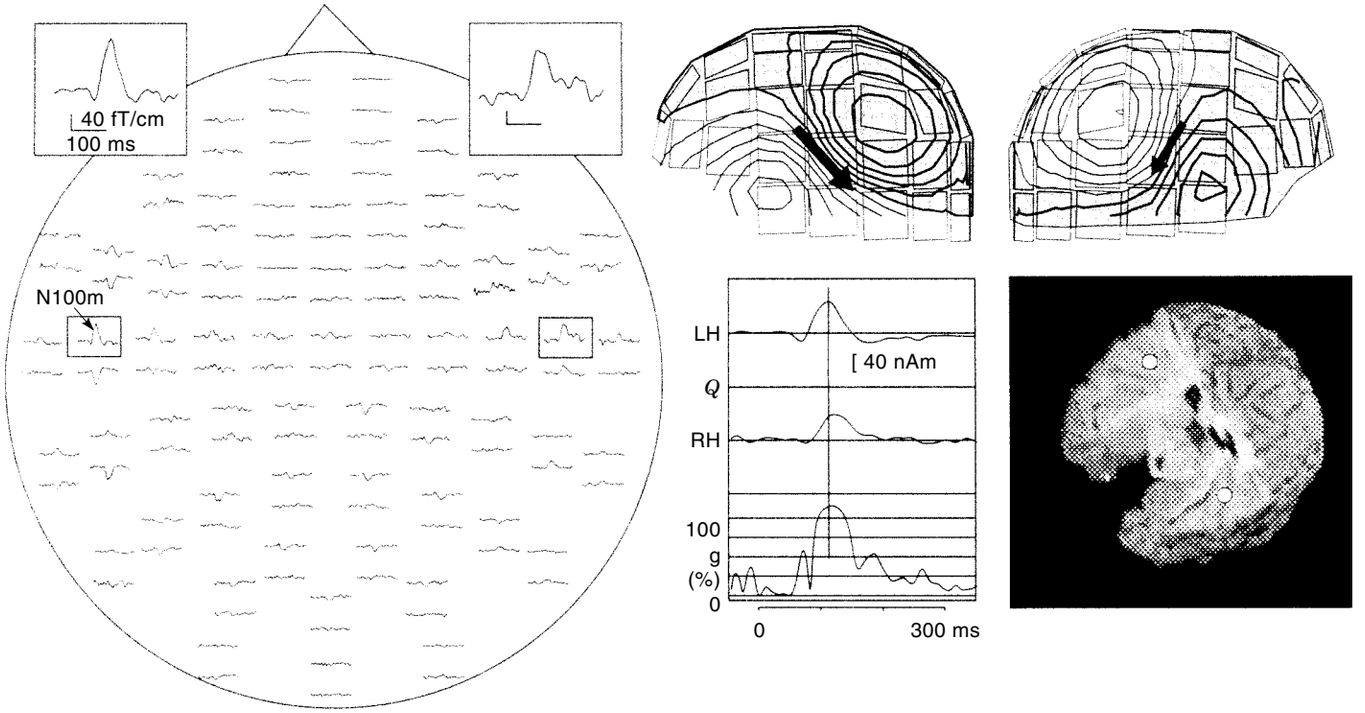

Figure 3. Left: Auditory evoked magnetic fields recorded with a 122-channel magnetometer (33) to 50 ms, 1 kHz tones presented to the subject's right ear once every 4 s. The head is viewed from above, and the helmet surface has been projected onto a plane; the nose points up. Right, above: The pattern of the field component normal to the helmet surface, B_z, shows the peak of the response. White indicates magnetic flux into and gray out of the head. The locations of the sensor units are indicated with squares. The positions and orientations of the two current dipoles modeling the data are projected to the helmet surface. Middle: Time dependence of the dipole strengths, indicating the time behavior of the active area in the left (LH) and right (RH) hemispheres. Q denotes the dipole moment; goodness-of-fit (g) indicates how well the model agrees with the measurement. Right, below: The locations of the dipoles projected on an MRI surface rendering, viewed from above. To show the supratemporal surface, frontal lobes have been removed from the images. (Modified from Ref. 83.)

from the subject's MRI data. The locations of the sources agree nicely with the known site of the auditory cortex on the supratemporal plane. Furthermore, the time courses of the source amplitudes show that the source in the left hemisphere, opposite to the stimulus, is stronger and peaks about 20 ms earlier than the source on the right.

Characterization of Cortical Rhythms and their Reactivity. Since the advent of EEG, the rhythmic oscillations of various cortical areas have been described and also utilized in clinical diagnosis, but their functional significance has remained unclear. With the whole-scalp neuromagnetometers, studies of cortical rhythms have become feasible. Because these rhythms do not repeat themselves, it is mandatory to record them simultaneously over the whole scalp.

The neuromagnetic brain rhythms in healthy adults have been recently characterized in (84) and their reactivity has been quantified during different situations. An efficient way to reveal task-related changes in the level of different frequency components is to filter the signal to the frequency passbands of interest, rectify it, and finally average the rectified signal with respect to the event of interest, like the onset of a voluntary movement (85).

Such an analysis has unraveled new features—for example, of the well-known mu rhythm, which is seen in the EEG records over the somatomotor cortices of an immobile subject. The comb shape of the mu rhythm already indicates the coexistence of two or three frequency components, strongest around 10 Hz and 20 Hz. The sources of the magnetic mu rhythm components cluster over the hand somatomotor cortex, with slightly more anterior dominance for the 20 Hz than for the 10 Hz cluster (see Fig. 4) (85). This difference suggests that the 20 Hz rhythm receives a major contribution from the precentral motor cortex, whereas the 10 Hz component seems mainly postcentral (somatosensory) in origin.

Further support for the functional segregation of these rhythms comes from their different reactivity to movements (15). The level of the 10 Hz rhythm starts to dampen 2 s before a voluntary movement and then returns back within 1 s after the movement. Suppression of the 20 Hz rhythm starts later and is relatively smaller, and the "rebound" after the movement is earlier and stronger than in the 10 Hz band.

Locating Epileptic Foci. Many patients with drug-resistant epilepsy suffer from seizures triggered by a small defective brain area. In preoperative evaluation of these patients, it is

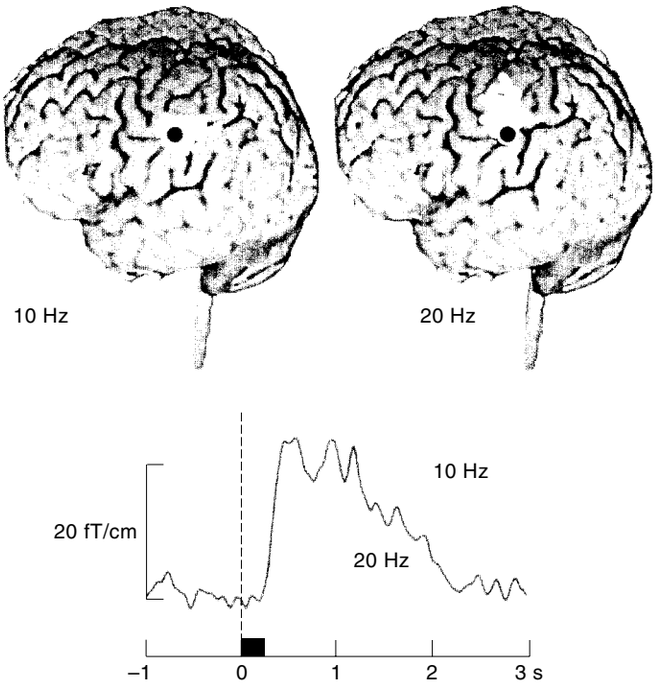

Figure 4. Reactivity of spontaneous activity over the somatomotor hand region in association with voluntary right index finger movements. The time dependencies of the 10 Hz and 20 Hz activities are indicated by the two traces showing the temporal spectral evolution (84) of the signal recorded over the left somatomotor hand area. The locations of sources corresponding to 10 Hz and 20 Hz activity are indicated on the 3 D surface rendition of the subject's magnetic resonance images. The site of the source for electrical stimulation of the median nerve at the wrist is shown by the black dot.

important to know whether their epileptic discharges are focal and how many brain areas are involved, what is the relative timing between the foci, and how close they are to functionally irretrievable locations such as the motor and speech areas. MEG recordings have been able to answer some of these questions (86,87). The patients cannot be studied with MEG during major seizures, owing to movement artifacts, but in many cases the foci can be identified from interictal discharges occurring during the periods between the seizures.

As an example of a recording during an actual seizure Fig. 5 depicts MES signals from a patient who suffered from convulsions in the left side of his face (88). He was able to trigger the seizure by touching the left-side lower gum with his tongue.

The recordings show clear epileptic spikes which appear only in the right hemisphere at first, but later start to emerge in the corresponding areas of the left hemisphere as well. After the 14 s seizure, the epileptic discharges ended abruptly. Figure 5 also depicts locations of the spike ECDs, superimposed on the patient's MRI surface rendering. The sources are clustered along the anterior side of the central sulcus, extending 1 cm to 3 cm lateral to the SI hand area, as determined by somatosensory median-nerve evoked responses. The sources of the epileptic spikes thus agree with the face representation area in the precentral primary motor cortex and are in accord with the patient's clinical symptoms. Spikes generated by the focus in the left hemisphere lagged behind the right-sided spikes by about 20 ms and probably reflected transfer of the discharges through corpus callosum from the primary to the secondary focus. Identification of secondary epileptogenesis is important for presurgical evaluation of patients because the secondary foci may with time become independent, and removal of the primary focus would then no longer be efficient in preventing the seizures.

Cardiac Studies

Ventricular Preexcitation. Ventricular preexcitation associated with the Wolff–Parkinson–White (WPW) syndrome is caused by an accessory pathway between the atria and the ventricles, which may lead to supraventricular tachycardias and life-threatening arrhythmias refractory to drug therapy. Intervention therapy, such as catheter ablation, is then needed, but a necessary condition for successful elimination of the premature conduction is the reliable localization of the accessory pathway.

Catheter ablation techniques have significantly decreased the need for cardiac surgery, but simultaneously increased the need for accurate noninvasive localization techniques. Noninvasively obtained prior knowledge of the site of the accessory pathway can improve the result and shorten the time needed in invasive catheter mapping, and thus diminish patient discomfort and surgical risk. In addition, shortening the time needed in invasive catheterization also reduces radiation exposure due to fluoroscopy monitoring of catheter positions.

Several MCG studies have been reported on localizing the ventricular preexcitation site in patients with the WPW syndrome (17,20,89,90). The reported accuracy of MCG localiza-

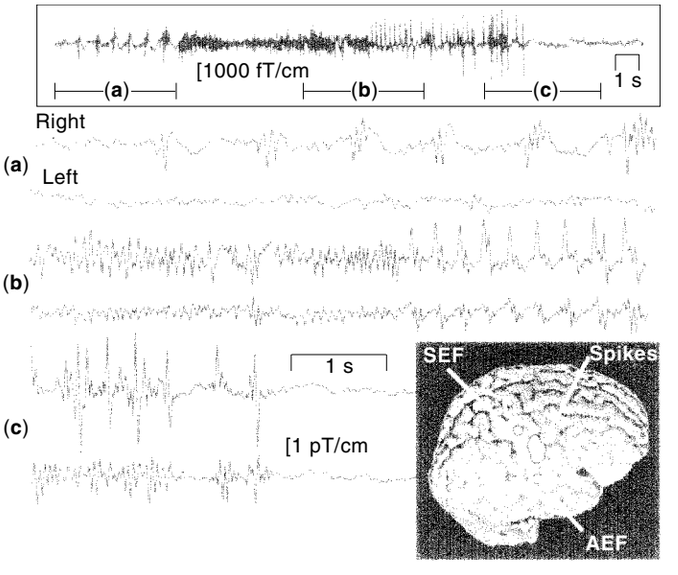

Figure 5. Epileptic discharges after voluntary triggering (88). The trace on the top illustrates MEG activity from the right hemisphere during the whole 14 s seizure. In the middle and lower parts of the figure, selected periods (a, b, c) are expanded and signals generated by the corresponding area in the left hemisphere are shown for comparison. Lower right corner: Locations of ECDs for ictal and interictal spikes (white cluster), and for auditory (AEF) and somatosensory (SEF) evoked fields, superimposed on the patient's MRI surface rendering. The course of the Rolandic and Sylvian fissures are indicated by the white dashed lines. (Adapted from Ref. 88.)

tions ranges from 5 mm to 25 mm, which is sufficient to be useful in preablative or presurgical consideration of the patients.

Ventricular Tachycardia. Generally, malignant ventricular tachycardia (VT) is much more difficult to locate for ablation treatment than the ventricular preexcitation. It is estimated that the lesion produced by the application of RF current is about 6 mm in diameter and about 3 mm in depth. Currently, clinical practice for precise localization introduces several catheters through arteries and veins into the ventricles for invasive recordings of cardiac activation sequences. This procedure can be very time-consuming, and noninvasively obtained information could shorten the procedure from several hours even to less than 1 hour.

VT patients include postmyocardial infarction patients, patients with different cardiomyopathies, and patients with monomorphic VT. MCG studies reported so far have attempted to locate the origin of ventricular extrasystoles or arrhythmias that have occurred spontaneously during the MCG recording (17,19,20). The results have been compared to the results of successful catheter ablations, presented over X-ray and magnetic resonance images when available. In such comparisons the average MCG locations were found to be within 2 cm from the invasively determined sites.

Examples of such studies are displayed in Fig. 6. These results were obtained with an individualized boundary-element torso model; an example is displayed in Fig. 7(a).

Cardiac Evoked Fields. Artificial dipole sources inserted in the heart with catheters (e.g., during routine electrophysiological studies) have been tested to verify the MCG localization accuracy (17,20,22). For example, Fenici et al. (22) studied five patients in whom a nonmagnetic pacing catheter (16) was used to stimulate the heart during MCG recordings. In general, the MCG localization results at the peak of 2 ms catheter stimuli and at the onset of paced myocardial depolarization were within 5 mm from each other. Because these are two physically different sources, the study provided further support for the good localization accuracy of the MCG method. In another recent study (91), simultaneous MCG and ECG mapping recordings were performed during pacing in 10 patients. The localizations were compared to catheter positions documented on fluoroscopic X-ray images. MCG results were, on the average, within 5 mm from the documented catheter position, while the ECG showed somewhat worse accuracy.

Reconstruction of Distributed Sources. For comparison of MCG and ECG mapping results, simultaneously recorded MCG and ECG data were applied in reconstructing ventricular depolarization isochrones on the endo- and epicardial surfaces of the heart of a healthy normal subject (92). The results showed almost identical isochrones from both magnetic and electric data. An example of the MCG isochrone reconstructions is shown in Fig. 6(d).

The minimum-norm estimates (MNE) have been applied in estimating the primary current distributions underlying measured MCG signals. An intrinsic problem associated with MNE is that it has a poor depth resolution of the sources without proper regularization and physiological constraints. Various regularization and depth weighting methods have shown promising results (21,69).

Recently, depth-weighted MNE reconstruction has been applied in MCG data recorded in patients with chronical myocardial ischemia (18,93). Clinical validation for the results was provided by SPECT imaging. In general, the site of smallest current density, i.e., the missing depolarization component, was in good agreement with the SPECT result.

OTHER APPLICATIONS

Until now, magnetic source imaging studies have been focused in the brain or the heart. However, other applications are being developed as well.

Studies of compound action fields (CAF) from peripheral nerves require a very high sensitivity, because the signal amplitudes are below 10 fT (94–97). In addition, signal averaging of hundreds of stimulated sequences may be required to find the CAF waveforms. Analysis of the waveforms demonstrates the quadrupolar nature of neural activity, provided that the observations are performed at a distance from the depolarized segment (96). Multipole analysis has been applied to model the depolarization process; dipole terms reveal the location and intensity of the source, while octupolar terms are related to its longitudinal extension along the nerve fibers. In addition to studying propagation of the nerve impulses, multichannel measurements can reveal abnormalities such as proximal conduction blocks in the spinal nervous system (97).

High sensitivity and specific signal processing are also needed to detect low-frequency (0.05–0.15 Hz) magnetic signals from gastrointestinal system (98,99). Distinguishing between gastric and small bowel signals may provide a new tool to study abnormalities in the gastrointestinal system (98). Multichannel recordings allow feasible and continuous monitoring of magnetically marked capsules within the gastrointestinal tract with a temporal resolution on the order of milliseconds and a spatial resolution within a range of millimeters (99).

DISCUSSION

Modeling

Despite the inevitable ambiguities in source analysis, very useful information has been obtained by using relatively simple models. For example, the localization of functional landmarks in the brain using the current dipole model and a spherically symmetric conductor in the forward calculations has already been developed to the extent of being a reliable clinical tool (16). The results of these studies have also been often verified in direct intraoperative recordings.

The focal source analysis methods are sometimes criticized for being too extreme simplifications of the actual current distributions, which renders them rather useless in the study of complicated functions performed by the human brain. This intuitively appealing opinion is not well backed up by experimental data. Rather, recent fMRI data may be taken to indicate that the significant changes in metabolic activity associated even with complicated cognitive tasks might well be relatively focal.

Reconstruction methods to deal with source distributions are under development, but there are still difficulties in interpretation of the results obtained from measured data. Implementation of available physiological information and constraints is probably needed to obain a reasonable correlation with actual physiological events in the source regions. If the assumptions of the source model are not compatible with the characteristics of the actual electrophysiological sources, misleading estimates may ensue. As discussed in the section entitled "Distributed Source Models," the distributed source model may produce a distributed estimate even for a focal source. Only very recently have there been attempts to reliably estimate the actual extent of the current source using Bayesian parameter estimation (100) in conjunction with reasonable physiological and anatomical constraints.

Invasively recorded cardiac signals, such as potentials measured during electrophysiological studies on epi- and endocardial surfaces, provide the golden standard for validation of the MCG/ECG inverse solutions. Even though patient populations studied by MCG before or during invasive catheterization are still relatively small, the localization studies of various cardiac arrhythmias have shown encouraging results. Multichannel systems and accurate combination of the results with cardiac anatomy have improved the accuracy to the order of 5 mm to 10 mm, which is sufficient to aid in planning the curative therapy of arrhythmia patients. Further valida-

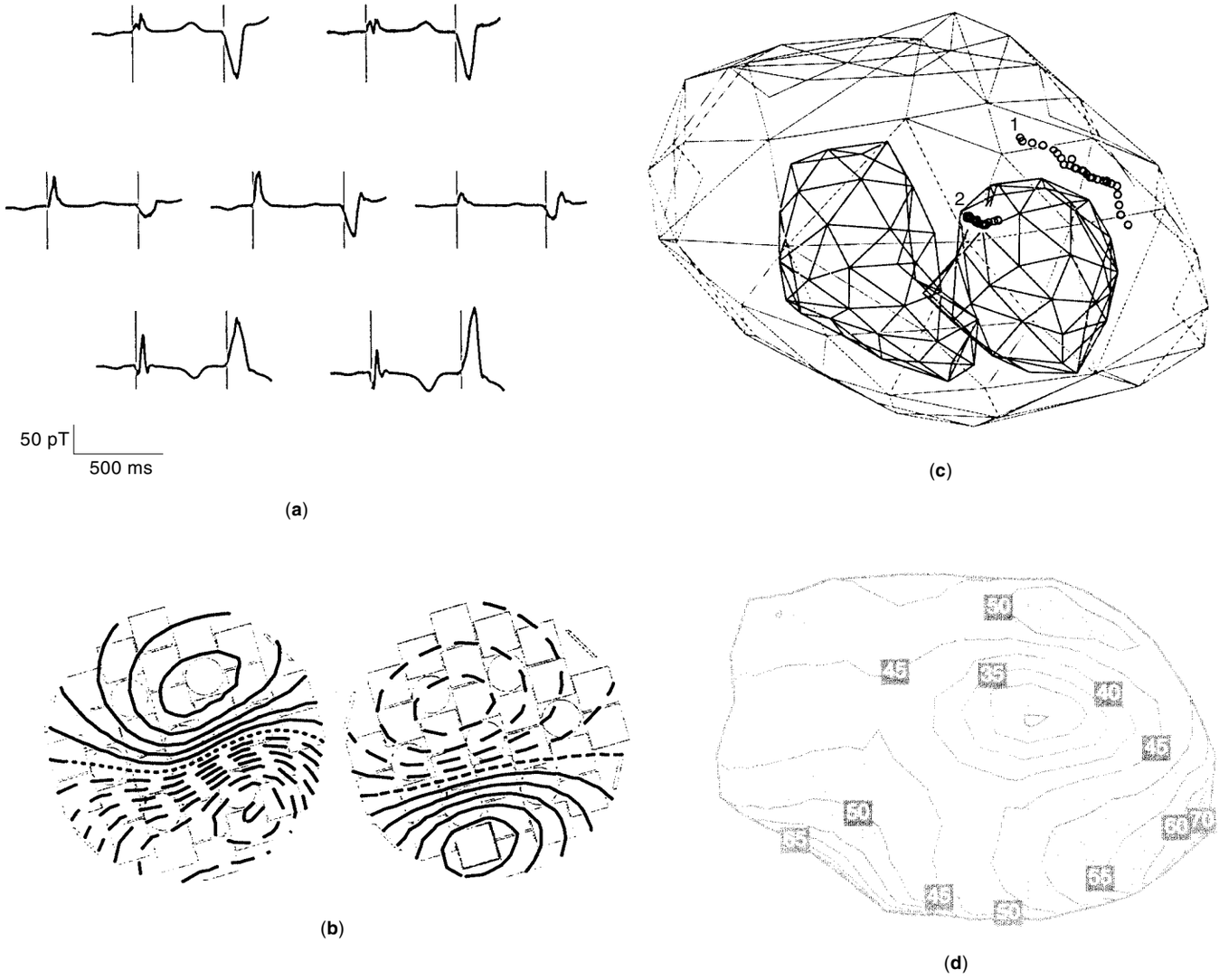

Figure 6. (a) MCG curves recorded from a patient suffering from ventricular tachycardia (VT). The seven axial gradiometers show (1) a normal sinus-rhythm beat and (2) an arrhythmogenic ventricular extrasystole (VES). (b) Isocontours of the magnetic-field component perpendicular to the sensor array (see Fig. 2). The field values were interpolated from the measured data with the minimum-norm estimation (68). Solid and dashed lines here indicate, respectively, magnetic flux toward or out of the chest. The step between adjacent contours is 1 pT. (c) MCG localization results obtained with a single moving ECD. (d) Ventricular activation sequence reconstructed from the VES by the method reported in Ref. 92.

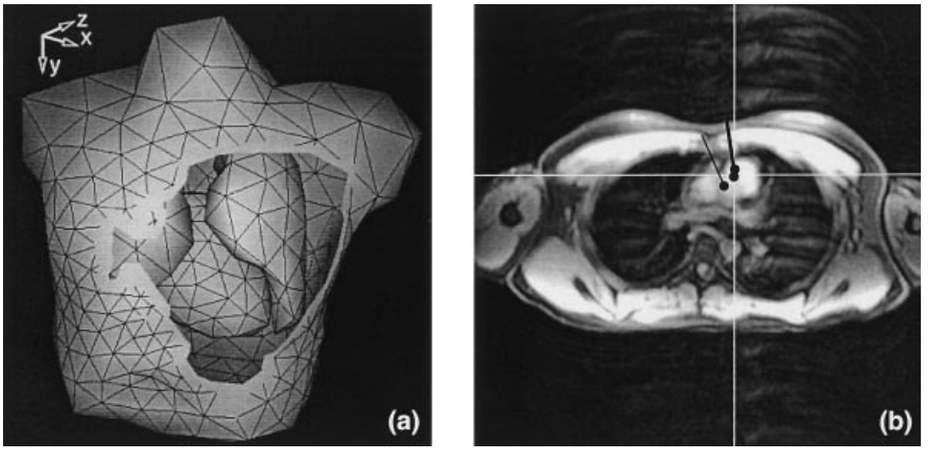

Figure 7. (a) An example of a boundary-element torso model constructed from MRI data. The surfaces of the body, the lungs, and the heart are tessellated into triangulated networks. The total number of triangles here is about 1500. (b) An example of MCG localization of tachycardias. The patient was suffering from continuous atrial tachycardia with the heart rate of over 140 beats per minute. ECD localization was performed from 67-channel MCG data at the onset of the P-wave, and the ECD locations were superimposed on the MRI data. Catheter ablation performed later at the location pinpointed by the MCG result terminated all arrhythmias.

tion for the MCG localization accuracy has been obtained by locating artificial dipole sources, such as pacing catheters inserted into the heart during electrophysiological studies.

Future Trends

The arrhythmogenic substrate is not manifested in all normal sinus rhythm recordings, and interventions may be needed during MCG to stimulate controlled arrhythmias to locate them. Thus, MCG should be available in a catheterization laboratory, but the demand of magnetical shielding and liquid helium is, in practice, limiting the use of MCG mapping in guiding invasive arrhythmia localization. For this purpose, compact-size higher-order magnetometer arrays operated without external shielding would be required.

MCG mapping under exercise is a promising tool for noninvasive characterization and localization of myocardial ischemia (76). Improved source modeling and localization methods are under test, especially in patients with coronary artery disease (93).

Despite over 20 years of MCG and MEG research, common standards of measurement techniques, data processing, and presentation are still lacking. Suggestions for such standards are emerging, but it is clear that there is and will be large differences between sensors and their arrangement in multichannel magnetometers. Fortunately, tools such as MNE (63,68) have been developed to interpolate signal morphologies and isocontour maps that are directly comparable to studies performed in other centers.

The field of magnetic source imaging may expand during the next few years with the implementation of low-noise high-T_c SQUID arrays that can be operated at the temperature of liquid nitrogen (101–103). The higher noise level of the high-T_c SQUIDs is, particularly in MEG studies, partly compensated by the smaller distance between the sensors and the body. At present, however, the low-T_c SQUIDs are easier to produce and thus cheaper than the high-T_c ones.

The future of MEG, with commercial whole-head instruments now available, looks promising. The capability to monitor activity of several cortical regions simultaneously in real time provides a unique window to study the neural basis of human cognitive functions. Important information can be obtained both from evoked responses and from spontaneous ongoing activity.

Effective signal processing and source modeling software is going to be increasingly important to extract all available functional data from the electromagnetic signals emerging from the brain and the heart. The widely discussed issue of whether the electric or magnetic technique is superior to the other is not of primary importance. Rather, one should apply a suitable alliance of different types of imaging methods, taking into account the characteristics and aims of the experiment being performed to yield optimal information about the functions of the biological system.

BIBLIOGRAPHY

1. G. Baule and R. McFee, Detection of the magnetic field of the heart, *Am. Heart J.,* **66**: 95–96, 1963.
2. D. Cohen, Magnetoencephalograpy: Evidence of magnetic fields produced by alpha-rhythm currents, *Science,* **161**: 784–786, 1968.
3. D. Cohen, E. A. Edelsack, and J. E. Zimmerman, Magnetocardiograms taken inside a shielded room with a superconducting point-contact magnetometer, *Appl. Phys. Lett.,* **16**: 278–280, 1970.
4. R. Hari and R. Ilmoniemi, Cerebral magnetic fields, *CRC Crit. Rev. Biomed. Eng.,* **14**: 93–126, 1986.
5. M. Hämäläinen et al., Magnetoencephalography—theory, instrumentation, and applications to noninvasive studies of the working human brain, *Rev. Mod. Phys.,* **65**: 413–497, 1993.
6. J. Nenonen, Solving the inverse problem in magnetocardiography, *IEEE Eng. Med. Biol.,* **13**: 487–496, 1994.
7. R. Näätänen, R. Ilmoniemi, and K. Alho, Magnetoencephalography in studies of human cognitive brain function, *Trends Neurosci.,* **17**: 389–395, 1994.
8. W. Andrae and H. Nowak (eds.), *Magnetism in Medicine,* Berlin: Wiley-VCH, 1998.
9. R. Hari, Magnetoencephalography as a Tool of Clinical Neurophysiology, in E. Niedermeyer and F. Lopes da Silva (eds.), *Electroencephalography: Basic Principles, Clinical Applications, and Related Fields,* 3rd ed., Baltimore, MD: Williams and Wilkins, 1993, pp. 1035–1061.
10. R. Salmelin et al., Dynamics of brain activation during picture naming, *Nature,* **368**: 463–465, 1994.
11. R. Salmelin et al., Impaired visual word processing in dyslexia revealed with magnetoencephalography, *Ann. Neurol.,* **40**: 157–162, 1996.

12. R. Näätänen et al., Language-specific phoneme representations revealed by electric and magnetic brain responses, *Nature,* **385**: 432–434, 1997.
13. R. Hari and R. Salmelin, Human cortical oscillations: A neuromagnetic view through the skull, *Trends Neurosci.,* **20**: 44–49, 1997.
14. C. Tesche et al., Characterizing the local oscillatory content of spontaneous cortical activity during mental imagery, *Cogn. Brain Res.,* **2**: 243–249, 1995.
15. R. Salmelin et al., Functional segregation of movement-related rhythmic activity in the human brain, *NeuroImage,* **2**: 237–243, 1995.
16. J. D. Lewine and W. W. Orrison, Magnetoencephalography, in W. G. Bradley and G. M. Bydder (eds.), *Advanced MR Imaging Techniques,* London: Martin Dunitz, 1997, pp. 333–354.
17. R. Fenici and G. Melillo, Magnetocardiography: Ventricular arrhythmias, *Eur. Heart J.,* **14** (Suppl. E): 53–60, 1993.
18. M. Mäkijärvi et al., New trends in clinical magnetocardiography, in C. Aine et al. (eds.), *Advances in Biomagnetism Research: Biomag96,* New York: Springer-Verlag, 1998 (in press).
19. M. Oeff and M. Burghoff, Magnetocardiographic localization of the origin of ventricular ectopic beats, *PACE,* **17**: 517–522, 1994.
20. W. Moshage et al., Evaluation of the non-invasive localization of cardiac arrhythmias by multichannel magnetocardiography (mcg), *Int. J. Cardiac Imaging,* **12**: 47–59, 1996.
21. G. Stroink, R. Lamothe, and M. Gardner, Magnetocardiographic and Electrocardiographic Mapping Studies, in H. Weinstock (ed.), *SQUID Sensors: Fundamentals, Fabrication and Applications,* Amsterdam: Kluwer Academic Publishers, 1996, NATO ASI Ser., pp. 413–444.
22. R. Fenici et al., Non-fluoroscopic localization of an amagnetic stimulation catheter by multichannel magnetocardiography, *PACE,* 1998, in press.
23. J. Montonen, Magnetocardiography in identification of patients prone to malignant arrhythmias, in C. Baumgartner et al. (eds.), *Biomagnetism: Fundamental Research and Clinical Applications,* New York: Springer-Verlag, 1995, pp. 606–611.
24. O. V. Lounasmaa, *Experimental Principles and Methods Below 1K,* London: Academic Press, 1974.
25. T. Ryhänen et al., SQUID magnetometers for low-frequency applications, *J. Low Temp. Phys.,* **76**: 287–386, 1989.
26. B. D. Josephson, Possible new effects in superconductive tunnelling, *Phys. Lett.,* **1**: 251–253, 1962.
27. J. Clarke, A superconducting galvanometer employing Josephson tunnelling, *Philos. Mag.,* **13**: 115, 1966.
28. J. Clarke, W. M. Goubau, and M. B. Ketchen, Tunnel junction dc SQUID fabrication, operation, and performance, *J. Low Temp. Phys.,* **25**: 99–144, 1976.
29. C. D. Tesche et al., Practical dc SQUIDs with extremely low 1/*f* noise, *IEEE Trans. Magn.,* **MAG-21**: 1032–1035, 1985.
30. D. Cohen, Magnetic measurement and display of current generators in the brain. Part I: The 2-D detector, *Dig. 12th Int. Conf. Med. Biol. Eng.,* Jerusalem, p. 15, 1979 (Petah Tikva, Israel: Beilinson Medical Center).
31. S. N. Erné and G. L. Romani, Performances of Higher Order Planar Gradiometers for Biomagnetic Source Localization, in H. D. Hahlbohm and H. Lubbig (eds.), *SQUID'85 Superconducting Quantum Interference Devices and their Applications,* Berlin: de Gruyter, 1985, pp. 951–961.
32. P. Carelli and R. Leoni, Localization of biological sources with arrays of superconducting gradiometers, *J. Appl. Phys.,* **59**: 645–650, 1986.
33. J. E. T. Knuutila et al., A 122-channel whole-cortex SQUID system for measuring the brain's magnetic fields, *IEEE Trans. Magn.,* **29**: 3315–3320, 1993.
34. D. Cohen, Low-field room built at high-field magnet lab, *Phys. Today,* **23**: 56–57, 1970.
35. S. N. Erné et al., The berlin magnetically shielded room (BMSR): Section B—performances, in S. N. Erné, H.-D. Hahlbohm, and H. Lubbig (eds.), *Biomagnetism,* Berlin: de Gruyter, 1981, pp. 79–87.
36. V. O. Kelhä et al., Design, construction, and performance of a large-volume magnetic shield, *IEEE Trans. Magn.,* **MAG-18**: 260–270, 1982.
37. J. Knuutila et al., Design considerations for multichannel SQUID magnetometers, in H. D. Hahlbohm and H. Lubbig (eds.), *SQUID'85: Superconducting Quantum Interference Devices and their Applications,* Berlin: de Gruyter, 1985, pp. 939–944.
38. S. N. Erné et al., The positioning problem in biomagnetic measurements: A solution for arrays of superconducting sensors, *IEEE Trans. Magn.,* **MAG-23**: 1319–1322, 1987.
39. R. Plonsey, *Bioelectric Phenomena,* New York: McGraw-Hill, 1969.
40. J. P. Wikswo, Jr., J. P. Barach, and J. A. Freeman, Magnetic field of a nerve impulse: First measurements, *Science,* **208**: 53–55, 1980.
41. J. P. Wikswo, Jr.,, Cellular magnetic fields: Fundamental and applied measurements on nerve axons, peripheral nerve bundles, and skeletal muscle, *J. Clin. Neurophysiol.,* **8**: 170–188, 1991.
42. J. Sarvas, Basic mathematical and electromagnetic concepts of the biomagnetic inverse problem, *Phys. Med. Biol.,* **32**: 11–22, 1987.
43. A. C. L. Barnard, I. M. Duck, and M. S. Lynn, The application of electromagnetic theory to electrocardiology. I. Derivation of the integral equations, *Biophys. J.,* **7**: 443–462, 1967.
44. D. B. Geselowitz, On the magnetic field generated outside an inhomogeneous volume conductor by internal current sources, *IEEE Trans. Magn.,* **MAG-6**: 346–347, 1970.
45. Z. Zhang, A fast method to compute surface potentials generated by dipoles within multilayer anisotropic spheres, *Phys. Med. Biol.,* **40**: 335–349, 1995.
46. M. S. Hämäläinen and J. Sarvas, Realistic conductivity geometry model of the human head for interpretation of neuromagnetic data, *IEEE Trans. Biomed. Eng.,* **36**: 165–171, 1989.
47. S. N. Erné et al., Modelling of the His–Purkinje Heart Conduction System, in H. Weinberg, G. Stroink, and T. Katila (eds.), *Biomagnetism: Applications & Theory,* New York: Pergamon, 1985, pp. 126–131.
48. J. Neonen et al., Magnetocardiographic functional localization using current multipole models, *IEEE Trans. Biomed. Eng.,* **38**: 648–657, 1991.
49. J. Nenonen et al., Magnetocardiographic functional localization using a current dipole in a realistic torso, *IEEE Trans. Biomed. Eng.,* **38**: 658–664, 1991.
50. B. N. Cuffin and D. Cohen, Magnetic fields of a dipole in speical volume conductor shapes, *IEEE Trans. Biomed. Eng.,* **BME-24**: 372–381, 1977.
51. B. M. Horacek, Digital model for studies in magnetocardiography, *IEEE Trans. Magn.,* **MAG-9**: 440–444, 1973.
52. C. Brebbia, J. Telles, and L. Wrobel, *Boundary Element Techniques—Theory and Applications in Engineering,* Berlin: Springer-Verlag, 1984.

53. J. Lötjönen et al., A triangulation method of an arbitrary point set selected from medical volume data, *IEEE Trans. Magn.,* **34**: 2228–2233, 1998.
54. H. Buchner et al., Inverse localization of electric dipole current sources in finite element models of the human head, *Electroencephalogr. Clin. Neurophysiol.,* **102**: 267–278, 1997.
55. H. Helmholtz, Ueber einige Gesetze der Vertheilung elektrischer Ströme in körperlichen Leitern, mit Anwendung auf die thierisch-elektrischen Versuche, *Ann. Phys. Chem.,* **89**: 211–233, 353–377, 1853.
56. D. W. Marquardt, An algorithm for least-squares estimation of nonlinear parameter, *J. Soc. Ind. Appl. Math.,* **11**: 431–441, 1963.
57. M. Scherg and D. von Cramon, Two bilateral sources of the late aep as identified by a spatiotemporal dipole model, *Electroencephalogr. Clin. Neurophysiol.,* **62**: 232–244, 1985.
58. M. Scherg, R. Hari, and M. Hämäläinen, Frequency-Specific Sources of the Auditory N19–P30–P50 Response Detected by a Multiple Source Analysis of Evoked Magnetic Fields and Potentials, in S. J. Williamson et al. (eds.), *Advances in Biomagnetism,* New York: Plenum, 1989, pp. 97–100.
59. K. Uutela, M. Hämäläinen, and R. Salmelin, Global optimization in the localization of neuromagnetic sources, *IEEE Trans. Biomed. Eng.,* **45**: 716–723, 1998.
60. P. Berg and M. Scherg, Sequential Brain Source Imaging: Evaluation of Localization Accuracy, in C. Ogura, Y. Coga, and M. Shimokochi (eds.), *Recent Advances in Event-Related Brain Potential Research,* Amsterdam: Elsevier, 1996.
61. J. C. Mosher, P. S. Lewis, and R. Leahy, Multiple dipole modeling and localization from spatiotemporal MEG data, *IEEE Trans. Biomed. Eng.,* **39**: 541–557, 1992.
62. T. E. Katila, On the current multipole presentation of the primary current distributions, *Nuovo Cimento,* **2D**: 660–664, 1983.
63. M. S. Hämäläinen and R. J. Ilmoniemi, Interpreting magnetic fields of the brain: Minimum-norm estimates, *Med. Biol. Eng. Comput.,* **32**: 35–42, 1994.
64. A. A. Ioannides, J. P. R. Bolton, and C. J. S. Clarke, Continuous probabilistic solutions to the biomagnetic inverse problem, *Inverse Problems,* **6**: 523–542, 1990.
65. R. D. Pascual-Marqui, C. M. Michel, and D. Lehmann, Low resolution electromagnetic tomography: A new method for localizing electrical activity in the brain, *Int. J. Physchopsysiol.,* **18**: 49–65, 1994.
66. A. van Oosterom et al., The magnetocardiogram as derived from electrocardiographic data, *Circ. Res.,* **67**: 1503–1509, 1990.
67. P. Hansen, Numerical tools for analysis and solution of fredholm integral equations of the first kind, *Inverse Problems,* **8**: 849–872, 1992.
68. J. Numminen et al., Transformation of multichannel magnetocardiographic signals to standard grid form, *IEEE Trans. Biomed. Eng.,* **42**: 72–77, 1995.
69. K. Pesola et al., Comparison of regularization methods when applied to epicardial minimum norm estimates, *Biomed. Tech.,* **42** (Suppl. 1): 273–276, 1997.
70. R. MacLeod and D. Brooks, Recent progress in inverse problems in electrocardiography, *IEEE Eng. Med. Biol.,* **17**: 73–83, 1998.
71. A. M. Dale and M. I. Sereno, Improved localization of cortical activity by combining EEG and MEG with MRI cortical surface reconstruction: A linear approach, *J. Cog. Neurosci.,* **5**: 162–176, 1993.
72. K. Matsuura and Y. Okabe, Selective minimum-norm solution of the biomagnetic inverse problem, *IEEE Trans. Biomed. Eng.,* **42**: 608–615, 1995.
73. K. Matsuura and Y. Okabe, A robust reconstruction of sparse biomagnetic sources, *IEEE Trans. Biomed. Eng.,* **44**: 720–726, 1997.
74. K. H. Uutela, M. S. Hämäaläinen, and E. Somersalo, Spatial and temporal visualization of magnetoencephalographic data using minimum-current estimates, *NeuroImage,* **5**: S434, 1997.
75. M. Fuchs et al., Possibilities of functional brain imaging using a combination of MEG and MRT, in C. Pantev (ed.), *Oscillatory Event-Related Brain Dynamics,* New York: Plenum Press, 1994, pp. 435–457.
76. K. Brockmeier et al., Magnetocardiography and 32-lead potential mapping: The repolarization in normal subjects during pharmacologically induced stress, *J. Cardiovasc. Electrophysiol.,* **8**: 615–626, 1997.
77. D. Cohen and B. N. Cuffin, A method for combining MEG and EEG to determine the sources, *Phys. Med. Biol.,* **32**: 85–89, 1987.
78. M. Fuchs et al., Improving source reconstructions by combining bioelectric and biomagnetic data, *Electroenceph. Clin. Neurophysiol.,* **107**: 93–111, 1998.
79. P. Colli-Franzone et al., Potential fields generated by oblique dipole layers modeling excitation wavefronts in the anisotropic myocardium. Comparison with potential fields elicited by paced dog hearts in a volume conductor, *Circ. Res.,* **51**: 330–346, 1982.
80. J. P. Wikswo, Jr., Tissue Anisotropy, the Cardiac Bidomain, and the Virtual Cathode Effect, in D. Zipes and J. Jalife (eds.), *Cardiac Electrophysiology: From Cell to Bedside,* 2nd ed., Orlando, FL: 1994, Saunders, pp. 348–361.
81. P. Reissman and I. Magnin, Modeling 3d deformable object with the active pyramid, *Int. J. Pattern Recognition & Artif. Intell.,* **11**: 1129–1139, 1997.
82. G. Simpson et al., Spatiotemporal Mapping of Brain Activity Underlying Visual Attention Through Integrated MEG, EEG, FMRI and MRI, in C. Aine et al. (eds.), *Advances in Biomagnetism Research: Biomag96,* Springer-Verlag, New York, 1998.
83. J. P. Mäkelä, Functional differences between auditory cortices of the two hemispheres revealed by whole-head neuromagnetic recordings, *Hum. Brain Mapp.,* **1**: 48–56, 1993.
84. R. Salmelin and R. Hari, Characterization of spontaneous MEG rhythms in healthy adults, *Electroencephalogr. Clin. Neurophysiol.,* **91**: 237–248, 1994.
85. R. Salmelin and R. Hari, Spatiotemporal characteristics of sensorimotor neuromagnetic rhythms related to thumb movement, *Neuroscience,* **60**: 537–550, 1994.
86. W. W. Sutherling and D. S. Barth, Neocortical propagation in temporal lobe spike foci on mangetoencephalography and electroencephalography, *Ann. Neurol.,* **25**: 373–381, 1989.
87. R. Paetau et al., Magnetoencephalographic localization of epileptic cortex—impact on surgical treatment, *Ann. Neurol.,* **32**: 106–109, 1992.
88. N. Forss et al., Trigeminally triggered epileptic hemifacial convulsions, *NeuroReport,* **6**: 918–920, 1995.
89. J. Nenonen et al., Noninvasive magnetocardiographic localization of ventricular preexcitation in wolff-parkinson-white syndrome using a realistic torso model, *Eur. Heart J.,* **14**: 168–174, 1993.
90. M. Mäkijärvi et al., Magnetocardiography: Supraventricular arrhythmias and preexcitation syndromes, *Eur. Heart J.,* **14** (Suppl. E): 46–52, 1993.
91. R. Fenici et al., Clinical validation of three-dimensional cardiac magnetic source imaging accuracy with simultaneous magnetocardiographic mapping, monophasic action potential recordings, and amagnetic cardiac pacing, *11th Int. Conf. Biomagnetism, Biomag98,* Abstracts, Sendai, 1998, p. 119.

92. T. Oostendorp, J. Nenonen, and G. Huiskamp, Comparison of inverse solutions obtained from ECG and MCG maps, *Proc. 18th Annu. Int. Conf. IEEE Eng. Med. Biol. Soc.,* pp. CD-rom, 1996.
93. U. Leder et al., Non-invasive biomagnetic imaging in coronary artery disease based on individual current density maps of the heart, *Int. J. Cardiol.,* **64**: 83–92, 1998.
94. L. Trahms et al., Biomagnetic functional localization of a peripheral nerve in man, *Biophys. J.* **55**: 1145–1153, 1989.
95. R. Hari et al., Multichannel Detection of Magnetic Compound action Fields of Median and Ulnar Nerves, *Electroenceph. Clin. Neurophysiol.,* **72**: 277–280, 1989.
96. I. Hashimoto et al., Visualization of a moving quadrupole with magnetic measurements of peripheral nerve action fields, *Electroenceph. Clin. Neurophysiol.,* **93**: 459–467, 1994.
97. B.-M. Mackert et al., Mapping of tibial nerve evoked magnetic fields over the lower spine, *Electroenceph. Clin. Neurophysiol.,* **104**: 322–327, 1997.
98. W. O. Richards et al., Non-invasive magnetometer measurements of human gastric and small bowel electrical activity, in C. Baumgartner et al. (eds.), *Biomagnetism: Fundamental Research and Clinical Applications,* New York: Springer Verlag, 1995, pp. 743–747.
99. W. Weitschies et al., High-resolution monitoring of the gastrointestinal transit of a magnetically marked capsule, *J. Pharm. Sci.* **86**: 1218–1222, 1997.
100. D. M. Schmidt, J. S. George, and C. C. Wood, Bayesian inference applied to the electromagnetic inverse problem, Tech. Report, Los Alamos National Laboratory, Los Alamos, LA-UR-97-4813.
101. D. Drung et al., Integrated $YBa_2Cu_3O_{7-x}$ magnetometer for biomagnetic measurements, *Appl. Phys. Lett.,* **68**: 1421–1423, 1996.
102. M. Burghoff et al., Diagnostic application of high-temperature SQUIDs, *J. Clin. Eng.,* **21**: 62–66, 1996.
103. J. M. ter Brake et al., A seven-channel high-T_c SQUID-based heart scanner, *Meas. Sci. Techn.,* **8**: 927–931, 1997.

Reading List

H. Weinberg, G. Stroink and T. Katila, Biomagnetism, in J. G. Webster (ed.), *Encyclopedia of Medical Devices and Instrumentation, Vol. 1,* New York: Wiley, 1988, pp. 303–322.

S. J. Williamson et al., *Advances in Biomagnetism,* New York: Plenum, 1989.

M. Hoke et al., *Biomagnetism: Clinical Aspects,* Amsterdam: Elsevier, 1992.

C. Baumgartner et al., *Biomagnetism: Fundamental Research and Clinical Applications,* New York: Springer-Verlag, 1995.

C. Aine et al., *Advances in Biomagnetism Research: Biomag96,* New York: Springer-Verlag, 1998.

M. S. HÄMÄLÄINEN
J. T. NENONEN
Helsinki University of Technology